RSC Advances

PAPER

View Article Online
View Journal | View Issue



Cite this: *RSC Adv.*, 2022, **12**, 5374

# Praseodymia–titania mixed oxide supported gold as efficient water gas shift catalyst: modulated by the mixing ratio of oxides†

Weixuan Zhao,‡[a] Junjie Shi, ‡*[ab] Mingyue Lin,[cd] Libo Sun,[a] Huijuan Su,[a] Xun Sun,[a] Toru Murayama [aef] and Caixia Qi *[a]

Modulating the active sites for controllable tuning of the catalytic activity has been the goal of much research, however, this remains challenging. The O vacancy is well known as an active site in reducible oxides. To modify the activity of O vacancies in praseodymia, we synthesized a series of praseodymia–titania mixed oxides. Varying the Pr : Ti mole ratio (2 : 1, 1 : 2, 1 : 1, 1 : 4) allows us to control the electronic interactions between Au, Pr and Ti cations and the local chemical environment of the O vacancies. These effects have been studied study by X-ray photoelectron spectroscopy (XPS), CO diffuse reflectance Fourier transform infrared spectroscopy (CO-DRIFTS) and temperature-programmed reduction (CO-TPR, $H_2$-TPR). The water gas shift reaction (WGSR) was used as a benchmark reaction to test the catalytic performance of different praseodymia–titania supported Au. Among them, Au/$Pr_1Ti_2O_x$ was identified to exhibit the highest activity, with a CO conversion of 75% at 300 °C, which is about 3.7 times that of Au/$TiO_2$ and Au/$PrO_x$. The Au/$Pr_1Ti_2O_x$ also exhibited excellent stability, with the conversion after 40 h time-on-stream at 300 °C still being 67%. An optimal ratio of Pr content (Pr : Ti 1 : 2) is necessary for improving the surface oxygen mobility and oxygen exchange capability, a higher Pr content leads to more O vacancies, however with lower activity. This study presents a new route for modulating the active defect sites in mixed oxides which could also be extended to other heterogeneous catalysis systems.

Received 23rd November 2021
Accepted 1st February 2022

DOI: 10.1039/d1ra08572g

rsc.li/rsc-advances



## 1. Introduction

Metal oxides as one of the largest families of heterogeneous catalysts play a very important role in both industry application and academic research.[1–6] The varieties in compositions, electronic and geometrical structures lead to a broad spectrum of chemical properties. Among them, redox ability is considered as the key characteristic of metal oxides which determines the activities in heterogeneous catalysis.[1,5,7] The reducible oxides are usually considered as more active for the redox reactions, such as the CO oxidation, water gas shift reactions (WGSR) and reforming reactions.[2,8] In most cases the reducible oxides follow a Mars–van Krevelen (MvK) mechanism in reaction.[1,5,9] The key of the MvK mechanism is O from the oxide lattice can be removed and refilled.[1,10] The fast O exchange ability is therefore considered as a prerequisite for high activity.

Praseodymium oxide similar to ceria contains a mixed-valence state ($Pr^{4+}/Pr^{3+}$), which is reported to have the highest O mobility among the rare earth oxides (REOs) holds great promise in catalysis.[10–15] Our recent work on Au/$PrO_x$ shows praseodymia is rich in O vacancies can facilitate $H_2O$ dissociation in the WGSR. However, the reactivity of Au/$PrO_x$ is not as high as expected (several times higher than Au/$CeO_2$), although it has a relatively high O vacancy ratio (0.32).[12] Zhou *et al.* also find the catalytic performances of some catalysts are not always increase with the concentration of O defects.[16,17] One possible reason is that not all the O vacancies are the active sites, only those can balance the easy adsorbing of reactant molecules and

[a]*Shandong Applied Research Centre of Gold Nanotechnology, School of Chemistry & Chemical Engineering, Yantai University, Yantai 264005, China. E-mail: qicx@ytu.edu.cn; junjieshiding@gmail.com*

[b]*Department of Chemical Engineering, University of Florida, Gainesville, Florida 32611, USA*

[c]*Shanghai Environmental Protection Key Laboratory on Environmental Standard and Risk Management of Chemical Pollutants, East China University of Science and Technology, Shanghai 200237, China*

[d]*State Environmental Protection Key Laboratory of Environmental Risk Assessment and Control on Chemical Process, School of Resources and Environmental Engineering, East China University of Science and Technology, Shanghai, China*

[e]*Research Center for Gold Chemistry, Department of Applied Chemistry for Environment, Graduate School of Urban Environmental Sciences, Tokyo Metropolitan University, 192-0397 Tokyo, Japan*

[f]*Research Center for Hydrogen Energy-based Society, Department of Applied Chemistry for Environment, Graduate School of Urban Environmental Sciences, Tokyo Metropolitan University, Tokyo 192-0397, Japan*

† Electronic supplementary information (ESI) available. See DOI: 10.1039/d1ra08572g

‡ These authors contributed equally to this work.

desorbing of product molecules are the active sites.[17] In fact, both the STM and DFT studies already prove that the O vacancies can be divided into different types according to their arrangements.[18,19] For example, in the $CeO_2$ single crystal, O vacancies are in the forms of an isolated single point, linear clusters and triangular trimers, which also correspond to different activities and stabilities.[20]

One of the benchmark reactions that is usually used for testing the O vacancies activities is the WGSR. Due to O vacancies on the oxide play a crucial role in facilitating $H_2O$ dissociation (limiting step) for the WGSR (Fig. 1).[21] In addition, WGSR is known as an essential process for hydrogen generation and CO removal in various energy-related chemical operations.[21–26] Recently, its potential application in proton-exchange membrane fuel cells (PEMFCs) for eliminating CO and simultaneously producing hydrogen has aroused great interest, especially after the discovery of gold/oxide system shows high performance for the low temperature (200–300 °C) WGSR by Flytzani-Stephanopoulos and co-workers. They proposed that the atomically dispersed nonmetallic Au or Pt is the active site for the WGSR. Inspired by this study, recently the single-site catalysts have become a very active frontier of heterogeneous catalysis.[22,24–29]

In order to further improve the efficiencies of supported catalyst, many attentions have been paid to synthesize single active site or modify the chemical environment of O vacancies on an oxide support.[26,30–34] One effective way to modulate the local environment of the O vacancy is by doping heteroatoms.[1,3,5,6] The substitution of a metal cation with another dopant will result in a direct change in the chemical environment and electronic structure of oxide.[8] According to Stacchiola *et al.*, the $Ti^{4+}$ cations dopant can decrease the O vacancy formation energy in ceria, therefore leads to easier reduction of ceria–titania mixed oxides.[6] The theoretical study indicates the incorporation of Ti into ceria induces half of the oxygen ions moving toward $Ti^{4+}$ and the other half away from $Ti^{4+}$ in $Ce_{0.8}Ti_{0.2}O_2$ and high degrees of strain are introduced to the bulk lattices.[6] The recent study on Pr–$TiO_x$/nanoporous gold (npAu) shows Pr–$TiO_x$ mixed oxides functionalized npAu exhibits higher catalytic activity than $PrO_x$/npAu and $TiO_x$/npAu for the WGSR.[11] Inspired by the inverse design catalyst, we are questioning if the Pr–$TiO_x$ mixed oxides supported Au can also show better catalytic activities in the WGSR in Fig. 1.[15,35] As praseodymium oxide is rich in O vacancies, the praseodymia–titania mixed oxides are a good system to study these relationships between O vacancies chemical environment and catalytic activities, to the best of our knowledge, this has been rarely studied.

In this work, we employed a sol–gel method for preparing praseodymia–titania mixed oxides. Gold was then loaded using a modified deposition–precipitation method. The catalytic activity of Au/$Pr_aTi_bO_x$ for the WGSR was studied in a plug-flow reactor. The structure of the catalysts was investigated with high-resolution transmission electron microscopy (HRTEM), high-angle annular dark-field imaging (HAADF) and energy-dispersive X-ray fluorescence (EDX) elemental mapping. The interactions of metal and support, as well as the metal cations inside the mixed oxides were examined by X-ray photoelectron (XPS) and CO diffuse reflectance Fourier transform infrared spectroscopy (CO-DRIFTS), which also gives information on changes in the chemical environment. The temperature-programmed desorption/reduction (CO-TPR, $H_2$-TPR) were used to evaluate the surface oxygen exchange capability and reducibility of catalysts which was closely related to the reactivity of the surface O vacancy site. Altogether, this enabled us to explain the origin of the doping ratio's effect of mixed oxides on catalytic performance and to illustrate the importance of the special chemical environment of O vacancies in promoting the limiting step of $H_2O$ dissociation.

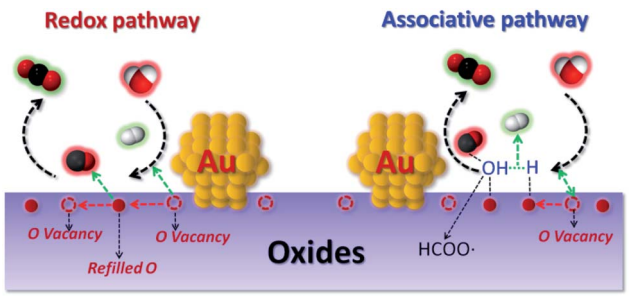


Fig. 1 Schematic illustration of the redox and associative pathway with redox regeneration for the WGSR at metal/oxide interface sites.

## 2. Experimental

### 2.1 Catalyst preparation

**2.1.1 Synthesis of $Pr_aTi_bO_x$.** Praseodymia–titania mixed oxides (denote as $Pr_aTi_bO_x$) were prepared *via* a sol–gel method reported previously. Typically, 1.5 mL TBOT (tetrabutyl-orthotitanate, Sinopharm Chemical Reagent Co., purity 98%) was added to absolute ethanol (200 mL, Sinopharm Chemical Reagent Co., purity 99.5%) under stirring for 15 min at room temperature. The desired amount of $Pr(NO_3)_3$ precursor solution (1 mol $L^{-1}$, Meryer Chemical Technology Co., purity 99.5%) was added drop-wise to above solution and stirred for 15 min. After adding 0.6 mL concentrated ammonia solution (Tianjin Kermel Chemical Reagent Co., concentration 28 vol%) a stack solution was formed and leaving it stirred for 24 h. Praseodymia–titania mixed hydroxides were obtained after drying for 12 h at 80 °C. Finally, the mixed hydroxides were calcined at 400 °C (heating rate: 3 °C $min^{-1}$) for 4 h in a muffle furnace to get the praseodymia–titania mixed oxides ($Pr_1Ti_2O_x$). The other mole ratios of Pr/Ti ($a/b$ = 0, 1/4, 1/1, 2/1) mixed oxides were prepared following the same procedure.

**2.1.2 Synthesis of Au/$Pr_aTi_bO_x$ catalysts.** Au was loaded on $Pr_aTi_bO_x$ through a modified deposition–precipitation (MDP) method. In brief, 0.3 g of $Pr_1Ti_2O_x$ powder was added to a $HAuCl_4$ (0.313 mL, Sinopharm Chemical Reagent Co., 9.56 g $L^{-1}$) and KOH mixed aqueous solution (Sinopharm Chemical Reagent Co., 85%, 1 mol $L^{-1}$) in a beaker. The pH was maintained at around 9 by KOH solution (yielding a nominal Au

loading of 1 wt%). The above solution was aged for 3 h then adding 20 mL ammonia solution (pH = 9) to remove $Cl^-$. Subsequently, the suspended solution was filtered, washed, and dried at 60 °C overnight. The resulting sample was denoted as $Au/Pr_aTi_bO_x$. The other samples $Au/TiO_2$, $Au/PrO_x$ were synthesized in the same way.

### 2.2 Catalyst characterization

Powder X-ray diffraction (XRD) analysis was carried out on a Rigaku SmartLab III using Cu Kα radiation ($\lambda = 1.54184$ Å, 40 mA and 40 kV) with a $2\theta$ angle ranging from 10° to 80° and a scanning rate of 10° $min^{-1}$. The gold content of in all catalysts was measured using an inductively coupled plasma-optical emission spectrometer (ICP-OES) with Agilent 5110 analyzer. The nitrogen adsorption–desorption isotherms were determined at −196 °C on a Micromeritics ASAP2020HD with pretreatment at 200 °C under vacuum for 3 h. Brunauer–Emmett–Teller (BET) equation was used to calculate the specific surface area. Pore size distribution was obtained from the desorption branch using the Barrett–Joyner–Halenda (BJH) method. Transmission electron microscopy (TEM) images and high-resolution TEM (HRTEM) images were performed on an FEI Talos F200X at an accelerating voltage of 200 kV. X-ray photoelectron spectra (XPS) measurements were recorded on a Thermo Scientific Escalab 250Xi equipped with Al Kα radiation (1486.6 eV). All binding energies were calibrated with the C 1s peak at 284.8 eV.

Pulse CO chemisorption carried out on Micromeritics AutoChem II 2920 was used to get the dispersion of Au. Prior to chemisorption, the catalysts were treated in the reaction gas (2 vol% CO and 10 vol% $H_2O$, $N_2$ balance) at 300 °C for 2 h and then in a nitrogen stream at 200 °C for 90 min to remove the adsorbed reaction gases, followed by cooling down to room temperature in Ar.

To be noticed, the samples were first treated in the reaction gas (2 vol% CO and 10 vol% $H_2O$) at 300 °C for 2 h to stabilize their chemical state, and about 100 mg of catalysts were used for the following experiments. Hydrogen temperature-programmed reduction ($H_2$-TPR) was measured on a Micromeritics AutoChem II 2920 apparatus with a thermal conductivity detector (TCD). In a typical process, about 100 mg of catalysts were sealed in a quartz tube reactor and purged in He (50 mL $min^{-1}$) atmosphere at 200 °C for 90 min to remove impurities on the surface. Then, the temperature was raised to 300 °C and pretreated in 20 vol% $O_2$/He (50 mL $min^{-1}$) for 60 min. After cooling down to room temperature, the analysis was carried out in a stream of 10 vol% $H_2$/He (50 mL $min^{-1}$) with a ramping rate of 10 °C $min^{-1}$ up to 800 °C.

The temperature-programmed CO reduction (CO-TPR) was carried out in Bel Cata II. A Bel mass spectrometer was used to monitor $CO_2$ ($m/z = 44$) and $H_2$ ($m/z = 2$) formation at the exit.

Table 1 Physicochemical properties of catalysts

| Samples | ICP Au loading (wt%) | $S_{BET}$ ($m^2$ $g^{-1}$) | XPS | | |
|---|---|---|---|---|---|
| | | | Pr (atomic%) | Ti (atomic%) | Pr : Ti real ratio |
| $Au/TiO_2$ | 0.69 | 104 | — | 18.1 | — |
| $Au/Pr_1Ti_4O_x$ | 0.46 | 135 | 2.5 | 7.5 | 1 : 3.0 |
| $Au/Pr_1Ti_2O_x$ | 0.61 | 105 | 4.7 | 7.7 | 1 : 1.6 |
| $Au/Pr_2Ti_1O_x$ | 0.24 | 2 | 4.9 | 2.7 | 1.8 : 1 |

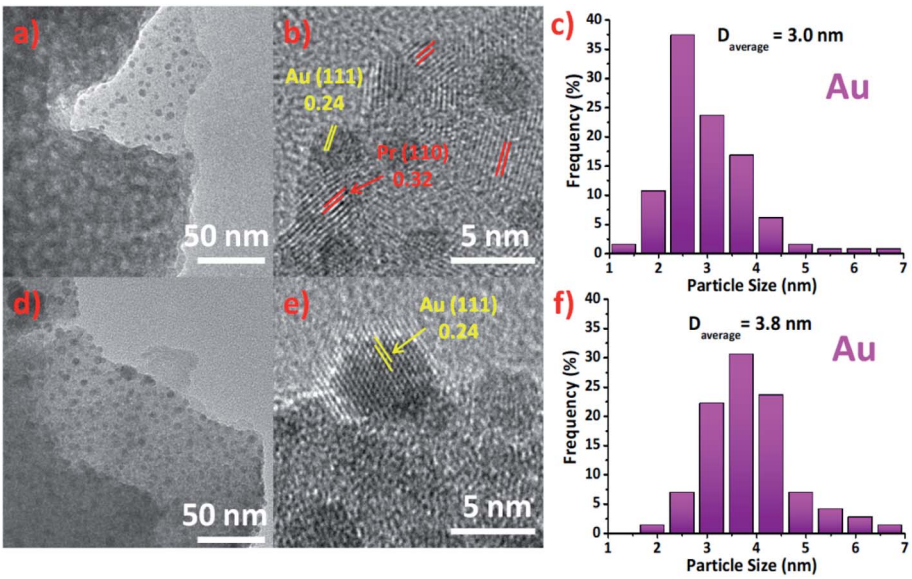


Fig. 2 TEM and HRTEM micro-graphs of $Au/Pr_1Ti_2O_x$ (a and b) and $Au/Pr_2Ti_1O_x$ (d and e). The size distributions of Au nano-particles for $Au/Pr_1Ti_2O_x$ and $Au/Pr_2Ti_1O_x$ are shown in (c and f), respectively. Images acquired after more than 10 h WGSR from 150 °C to 400 °C (feed-gas mixture: 2 vol% CO, 10 vol% $H_2O$, $N_2$ as carrier gas; total gas flow 45 mL $min^{-1}$).

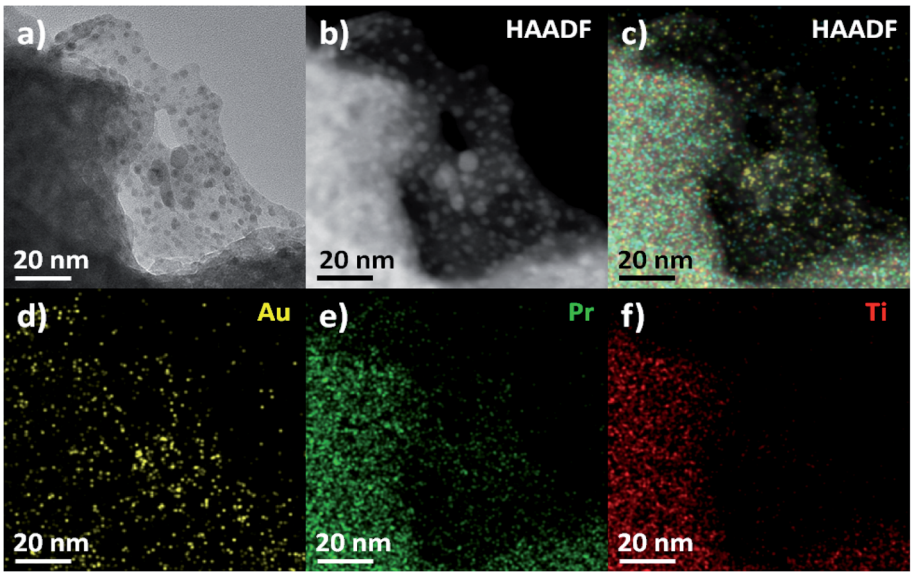


Fig. 3 (a) TEM and (b) HAADF-STEM image of Au/$Pr_1Ti_2O_x$, (c–f) elemental distributions maps. Au (yellow), Pr (green), Ti (red).

The catalysts were pretreated in He (30 mL $min^{-1}$) atmosphere at 200 °C for 90 min and then oxidized in 20 vol% $O_2$/He (30 mL $min^{-1}$) for 60 min. The analysis was carried out in a stream of 10 vol% CO/He (30 mL $min^{-1}$) from 50 to 800 °C at the rate of 10 °C $min^{-1}$.

CO-DRIFTS spectra were collected on a JASCO FT/IR-6100 spectrometer equipped with a diffuse reflectance accessory (ST Japan Heat Chamber HC-500) and MCT detector. CO-DRIFTs spectra were recorded by accumulating 128 scans with a resolution of 4 $cm^{-1}$. The sample was first purged under $N_2$ (50 mL $min^{-1}$) at the 120 °C for 1 h in the IR cell. After cooling down to −180 °C the background spectrum was recorded and subtracted. The CO adsorption was carried out at −180 °C with 3.84 vol% CO/He (50 mL $min^{-1}$) for 30 min. Then $N_2$ gas was introduced at −180 °C with a flow rate of 50 mL $min^{-1}$ for 30 min to fully exclude the gas phase and weakly adsorbed CO species.[36–38]

To be noted most of the characterizations are done for the spent catalyst in order to more precisely reflecting the properties of catalysts especially under steady-state conditions. According to McFarland and Metiu, heterogeneous catalytic reactions are run under steady-state conditions instead of at equilibrium.[2] It is difficult to accurately describe the catalytic performance of oxide catalysts using the property parameters of as-prepared catalysts, which are more likely to be in thermodynamic equilibrium during the preparation process.[2]

### 2.3 Catalyst evaluations

The water gas shift reaction (WGSR) was performed under atmospheric pressure in a continuous flow reactor and a temperature range within 150–400 °C. About 50 mg of powder catalysts were packed to quartz wool in a U-shaped tube reactor (8 mm I.D.). An online Agilent 7820A gas chromatograph was used to detect the gas composition in feed and product gas streams by a thermal conductivity detector (TCD). The catalysts without pretreatment were tested under the following condition: CO, 2 vol%; $H_2O$, 10 vol%; $N_2$ 88 vol%; total gas flow, 45 mL $min^{-1}$; gas hourly space velocity (GHSV), 54 000 mL $g_{cat}^{-1}$ $h^{-1}$. Water vapor was fed into the reactor by a temperature-controlled saturator. The evaluations were maintained for 30 min to obtain catalyst performance. Reaction kinetics and stability test were performed under the same reaction conditions as catalytic evaluations. The kinetic studies were carried out at differential reaction conditions and by changing the amount of catalysts the conversion rate was kept below 20%.

The CO conversion ($X_{CO}$) was quantified using an area normalization method and determined by the degradation of CO gas following the equation:

$$X_{CO} = \left(\frac{CO_{in} - CO_{out}}{CO_{in}}\right) \times 100\%$$

where $CO_{in}$ ($CO_{out}$) is the area percentage of CO concentration in inlet (outlet) gas composition.

The turnover frequencies (TOF) were calculated based on the following equation:

$$\text{TOF } (s^{-1}) = \frac{X_{CO} \times F_{CO} \times M_{Au}}{W_{cat} \times X_{Au} \times D_{Au}}$$

where $X_{CO}$ is the CO conversion, $X_{Au}$ is the Au loading in the catalyst, $F_{CO}$ is the CO flow rate per unit time, $D_{Au}$ is the dispersion of Au, $M_{Au}$ is the molar weight of Au (197 g $mol^{-1}$).

## 3. Results and discussion

### 3.1 Structural and morphological studies

XRD investigation shows that only anatase phase $TiO_2$ is present in the Au/$TiO_2$. No diffraction peaks correspond to either praseodymia or titania are observed in the praseodymia–titania mixed oxides supported Au, with a broad peak present at 30°, which indicates the praseodymia–titania mixed oxides

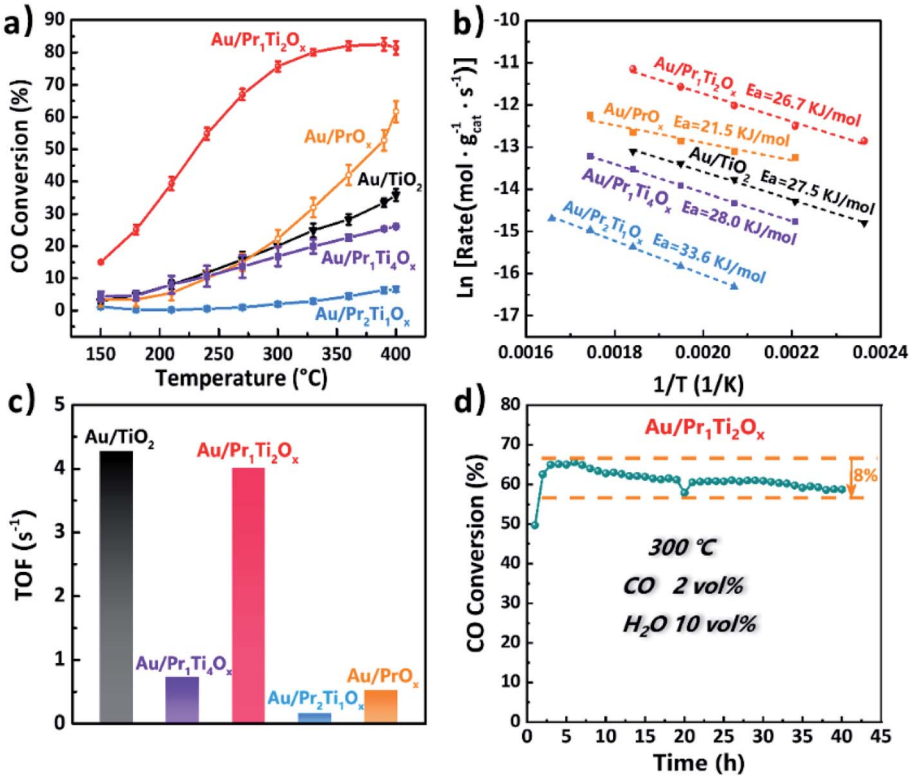


Fig. 4 (a) Steady-state test profiles of $Au/TiO_2$, $Au/PrO_x$ and $Au/Pr_aTi_bO_x$ catalysts for the WGS reaction (conditions: 2 vol% CO/10 vol% $H_2O/N_2$, 45 mL $min^{-1}$, $m_{catal}$ = 50 mg, space velocity 54 000 mL $h^{-1}$ $g_{cat}^{-1}$). (b) Arrhenius plots of WGSR over $Au/TiO_2$, $Au/PrO_x$ and $Au/Pr_aTi_bO_x$. The space velocity is much higher than in steady-state to ensure reaction within the kinetic regime (conversion of CO < 20%). (c) Histogram of TOF values at 300 °C determined on $Au/TiO_2$, $Au/PrO_x$ and $Au/Pr_aTi_bO_x$ catalysts for the WGS reaction. (d) Long-term catalytic evaluation at 300 °C for $Au/Pr_1Ti_2O_x$ (reaction conditions were the same as in steady-state).

mainly form an amorphous phase (Fig. S1†).[12,39] Moreover, no distinct peaks of gold particles are observed on all samples, demonstrating the high Au dispersion (Fig. S1†). The BET data in Table 1 shows that the specific surface areas of $Au/TiO_2$, $Au/Pr_1Ti_4O_x$ and $Au/Pr_1Ti_2O_x$ are in the range of 104–135 $m^2$ $g^{-1}$, while the $Au/Pr_2Ti_1O_x$ has a specific surface area of 2 $m^2$ $g^{-1}$. Such low surface area is also found on the $Au/Pr_1Ti_1O_x$ sample (2.3 $m^2$ $g^{-1}$, Table S1†), it reveals when the atomic ratio of praseodymium is over a half in the praseodymia–titania mixed oxides, the specific surface area will decrease sharply. The low surface area also leads to few exposed catalytic active sites, therefore low catalytic activity as indicated in catalytic performance (below). The bulk Au concentration measured by ICP-OES shows the Au loading varies from 0.46 wt% to 0.69 wt% on $Au/TiO_2$, $Au/Pr_1Ti_4O_x$ and $Au/Pr_1Ti_2O_x$, with $Au/Pr_2Ti_1O_x$ shows the lowest loading of 0.24 wt%, which can also be attributed to the low specific surface area of $Au/Pr_2Ti_1O_x$ result in few anchoring sites for Au. The XPS shows the surface atomic ratio of Pr : Ti for $Au/Pr_1Ti_4O_x$, $Au/Pr_1Ti_2O_x$ and $Au/Pr_2Ti_1O_x$ round 1 : 3, 1 : 1.6 and 1.8 : 1, respectively, which are close to the desired value (during synthesis), confirming the effectiveness of controlling the Pr : Ti ratio by using the sol–gel method.

TEM images in Fig. 2(a) and (d) corresponding to $Au/Pr_1Ti_2O_x$ and $Au/Pr_2Ti_1O_x$. As we can see the former can maintain the porous structure and nanosheet morphology, while the latter hardly have any pores. One explanation is that under the specific ratio (Pr : Ti = 2 : 1) the praseodymia–titania forming big aggregated particles. This is also in line with the nitrogen sorption analysis and explains why the $Au/Pr_2Ti_1O_x$ exhibit such a small specific surface area (Fig. S2†). The HRTEM images of $Au/Pr_1Ti_2O_x$ and $Au/Pr_2Ti_1O_x$ in Fig. 2(b) and (e) display interplanar spacings of 0.24 nm and 0.32 nm, corresponding to the (111) plane of Au and (110) plane of $Pr_6O_{11}$, respectively.[11,12,35,40–43] In addition, from Fig. 2(a) and (d) we can see the surface of nano-sheet are decorated with many small particles, which are attributed to be Au nanoparticles. The histogram analysis reveals that the Au nanoparticles have a mean size of about 3.0 ± 1.2 nm in the case of $Au/Pr_1Ti_2O_x$ (Fig. 2(c)) and slightly bigger size of around 3.8 ± 1.5 nm in the case of $Au/Pr_2Ti_1O_x$ (Fig. 2(f)). The Fig. 2(b) and (e) further indicates the arrangement of Au nanoparticles at the interfaces, with half of the Au atoms embedded into the supports. Similar to the observations on the nano-rod ceria supported Au catalyst, according to Shen *et al.*, the interfacial surface oxygen vacancies on oxide support work as anchoring sites for Au nanoparticles facilitating its stabilization.[44]

A combined TEM (Fig. 3(a)), high-angle annular dark-field (HAADF) STEM images (Fig. 3(b)) and energy-dispersive spectroscopy (EDS) mapping (Fig. 3(c)–(f)) were used to determine the distribution of different components in $Au/Pr_1Ti_2O_x$

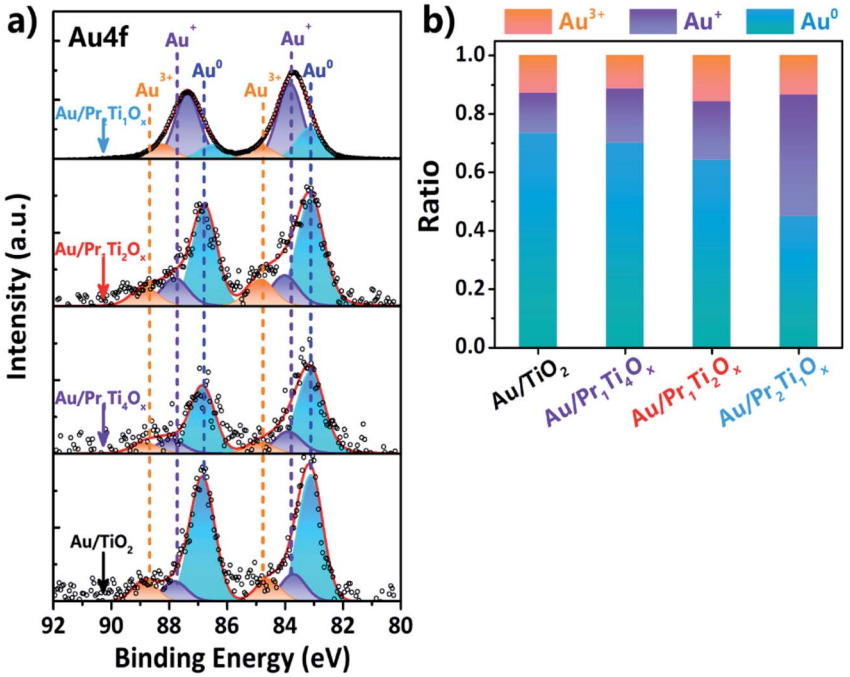


Fig. 5 Photoemission (XPS) spectra of (a) Au 4f over the Au/$Pr_aTi_bO_x$ and Au/$TiO_2$ catalysts after WGSR (2 vol% CO + 10 vol% $H_2O/N_2$, 10 h on-stream, 150 to 400 °C). (b) Plots of metallic and ionic Au ratios (peak area of $Au^0$/or $Au^{3+}$/or $Au^+$ to total peak area).

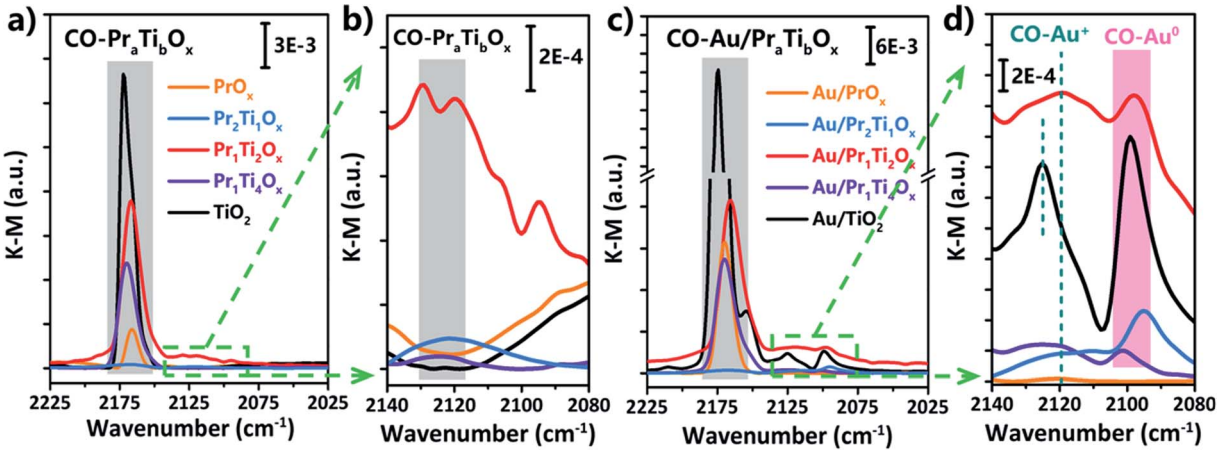


Fig. 6 DRIFT spectra of CO adsorption at −180 °C over the supports (a and b) and Au/$TiO_2$, Au/$PrO_x$, Au/$Pr_aTi_bO_x$ catalysts (c and d) after WGSR (2 vol% CO + 10 vol% $H_2O/N_2$, 10 h on-stream, 150 to 400 °C).

catalyst. The STEM-EDS mapping of Pr (Fig. 3(e)) and Ti (Fig. 3(f)) show a homogeneous distribution in the catalysts, indicates praseodymia was successfully mixed with titanium rather than separated mixture which is also in line with the XRD study. The signal of Au (Fig. 3(d)) corresponds well with the position of the nanoparticles in the HAADF-STEM (Fig. 3(b)), further confirming that they are Au nanoparticles.

### 3.2 Catalytic performance

Catalytic performances of the Au/$Pr_aTi_bO_x$ (Au/$Pr_1Ti_4O_x$, Au/$Pr_1Ti_2O_x$, Au/$Pr_1Ti_1O_x$ and Au/$Pr_2Ti_1O_x$) and Au/$TiO_2$ catalysts for WGSR were studied with a continuous flow reactor in the temperature range of 150–400 °C. The Au/$Pr_1Ti_2O_x$ sample (Fig. 4(a)) exhibits exceptional high activities among the catalysts in the whole temperature range. Already at temperatures of 150 °C the catalytic conversion of water and CO is observed (Fig. 4(a)) over Au/$Pr_1Ti_2O_x$ and around 15%. At 300 °C, the CO conversion rate over Au/$Pr_1Ti_2O_x$ reached the highest point (75%), which is about 3.2 times that of Au/$TiO_2$ (25%) and 2.7 times that of Au/$PrO_x$ (30%). The Au/$Pr_1Ti_1O_x$ (Fig. S4†) and Au/$Pr_2Ti_1O_x$ show very poor activity. Further increase the temperature to 400 °C instead leads to a slight decrease in the CO conversion rate. This is due to the WGSR is an exothermic reaction, at a high temperature which is thermodynamically

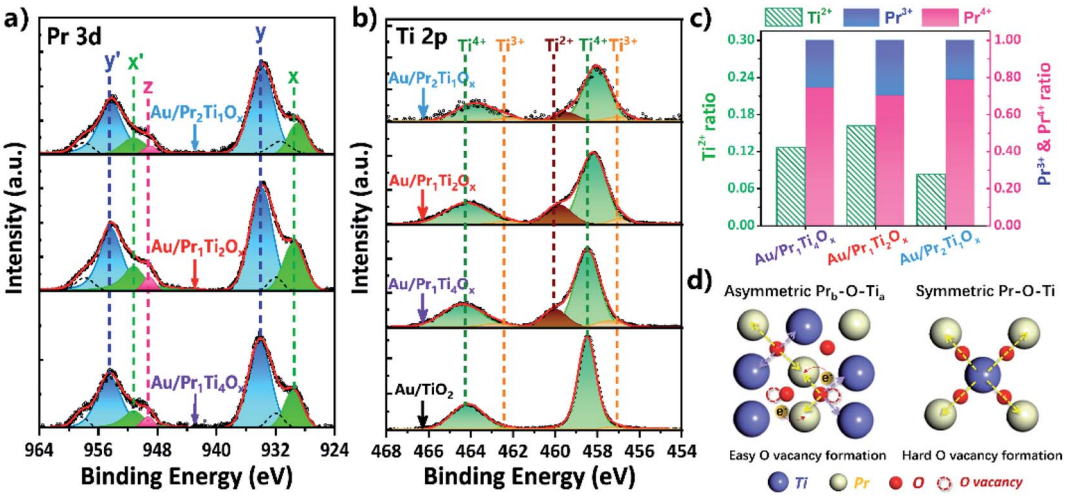


Fig. 7 XPS spectra of (a) Pr 3d, (b) Ti 2p of $Au/Pr_aTi_bO_x$ and $Au/TiO_2$ catalysts after WGSR (2 vol% CO + 10 vol% $H_2O/N_2$, 10 h on-stream, 150 to 400 °C) (the *x*/*x*′ and *z* can be ascribed to $Pr^{3+}$ and *y*/*y*′ corresponds to $Pr^{4+}$); (c) plots of $Ti^{2+}$, $Pr^{3+}$ and $Pr^{4+}$ ratios (peak area of $Ti^{2+}$/or $Pr^{3+}$/or $Pr^{4+}$ to total peak area); (d) schematic illustration of the formation of asymmetric site.

unfavorable.[25] In addition, after increasing or decreasing the atomic ratio of Pr in the praseodymia–titania mixed oxides corresponding to the $Au/Pr_2Ti_1O_x$ and $Au/Pr_1Ti_4O_x$ result in a drastically decrease in reactivity (Fig. 4(a)) of both catalysts. The control experiment pointed that pure $Pr_aTi_bO_x$ and $TiO_2$ were inactive for WGSR (CO conversion < 3%, 150–400 °C). We observed a similar behavior of catalysts in a simulate $CO_2$ laser conditioned CO oxidation ($CO_2$ 60 vol%, CO 1 vol%, $O_2$ 0.5 vol%, $H_2O$ 0.5 vol%, $N_2$ balanced) reaction, with the $Au/Pr_1Ti_2O_x$ shows the highest CO conversion rate of 75% at 120 °C, while $Au/Pr_1Ti_4O_x$ of 9% and $Au/Pr_2Ti_1O_x$ almost no reactivity at the same temperature (more details will be reported in another paper). The different behaviors of the catalysts suggest that the nature of the oxide support especially the atomic ratio of Pr : Ti plays a key role in determining the catalytic activities. Still, the high activity of $Au/Pr_1Ti_2O_x$ must be a result of a synergistic effect of Au species and the oxide support.

The apparent activation energy ($E_a$, Fig. 4(b)) amounts to 21.5, 26.7, 27.5, 28.0, 33.6 kJ $mol^{-1}$ for $Au/PrO_x$, $Au/Pr_1Ti_2O_x$, $Au/TiO_2$, $Au/Pr_1Ti_4O_x$ and $Au/Pr_2Ti_1O_x$, these values are comparable to the values reported by Fu *et al.* and Si *et al.*, with an $E_a$ of 37 kJ $mol^{-1}$ on $Au/CeO_2$ and 32 kJ $mol^{-1}$ on Au/(Ti–Ce)$O_2$ mixed oxides, respectively.[24,45] The relatively lower $E_a$ on $Au/Pr_1Ti_2O_x$ (26.7 kJ $mol^{-1}$) highlights the benefits of using $Pr_1Ti_2O_x$ mixed oxides as support.

The turn-over frequencies (TOF) were calculated to compare the WGSR activities with other reported catalysts. We assume that all Au atoms are active sites (Au dispersion measured by pulsed CO chemisorption). The bar plot in Fig. 4(c) displays the TOFs of the four catalysts at 300 °C. The order of TOFs follow the sequences of $Au/TiO_2$ (4.27 $s^{-1}$) > $Au/Pr_1Ti_2O_x$ (4.02 $s^{-1}$) > $Au/Pr_1Ti_4O_x$ (0.72 $s^{-1}$) > $Au/Pr_2Ti_1O_x$ (0.15 $s^{-1}$). The calculated TOF of $Au/Pr_1Ti_2O_x$ is around 4.02 $s^{-1}$ (300 °C), which is even higher than the nanoparticulate $Au/CeO_2$ (1.27 $s^{-1}$, at 350 °C) reported by Fu *et al.*[24]

In addition, we also tested the long-term stability of $Au/Pr_1Ti_2O_x$ for WGSR at 300 °C under steady-state conditions. As one major obstacle that limiting the practical applications of Au-based catalysts is rapid deactivation caused by aggregation of Au species and/or blocking of the active sites with the accumulation of intermediates (carbonates).[12,35,42,46] As indicated in Fig. 4(d), after 40 h continued time-on-stream test, the CO conversion rate only decreased from 65% to 57%. Compared with the reported catalysts so far, the $Au/Pr_1Ti_2O_x$ is among the most stable catalysts.[44] For example, Jia *et al.* found the reactivity of $Au/CeO_x$ decreased from 83% to 59% within 50 h even at lower *T* (250 °C).[22]

### 3.3 Investigations of electronic metal–support interaction

Fig. 5(a) shows the XPS spectra of Au 4f which is deconvoluted using a Gaussian fitting method. Two major peaks centered at 83.1 (Au $4f_{7/2}$) and 86.8 eV (Au $4f_{5/2}$) can be assigned to $Au^0$.[47] The amounts of $Au^0$ are higher than 40% in all the samples after reaction as a result of the strong reducing atmosphere of WGSR, which is also in line with the findings of Si *et al.*[45,48] The binding energy at 84.6 (Au $4f_{7/2}$) & 88.3 (Au $4f_{5/2}$) eV and 83.8 (Au $4f_{7/2}$) & 87.7 (Au $4f_{5/2}$) eV can be attributed to $Au^{3+}$ and $Au^+$, respectively.[47,49] From Fig. 5(b) we can see the amount of ionic Au ($Au^+$, 0.20; $Au^{3+}$, 0.16) in $Au/Pr_1Ti_2O_x$ is the higher compared with other samples ($Au/Pr_1Ti_4O_x$, 0.3; $Au/TiO_2$, 0.27). The positively charged Au indicates there is electron transfer from Au to the oxide ($Pr_aTi_bO_x$ and $TiO_2$) support. According to Buergel *et al.* the charge state of gold plays a key role in influencing the binding of CO molecules, with cationic gold clusters can promote the CO adsorption through both an Eley–Rideal-like and Langmuir–Hinshelwood-like mechanism.[50] In this work we demonstrate that by changing the oxide composition (Pr : Ti ratio) one can modify the electron transfer between the support and Au, therefore, control the content of ionic gold. This provides a new way to modulate the active sites in catalysts.

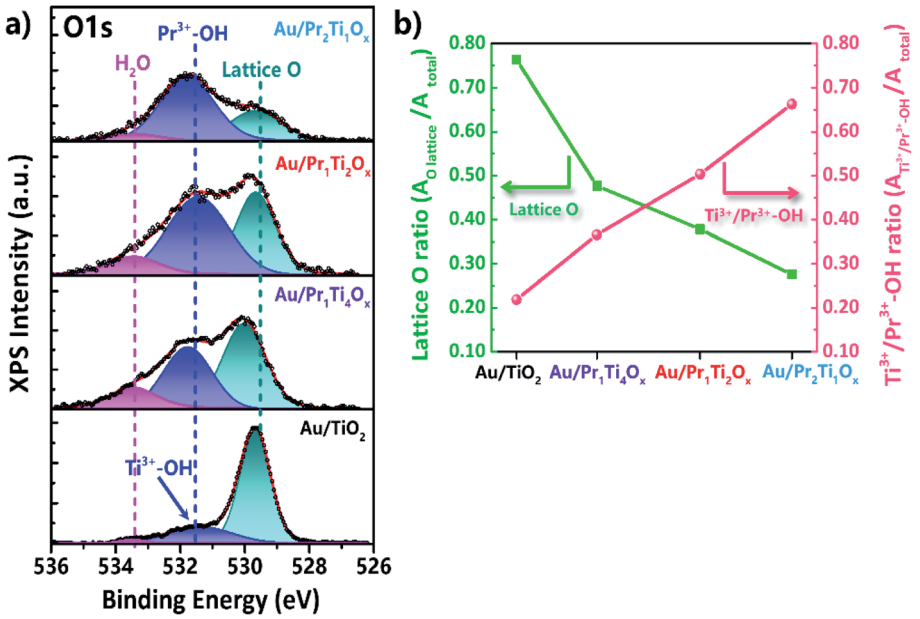


Fig. 8 Photoemission (XPS) spectra of (a) O 1s and (b) plots of lattice O and $Ti^{3+}/Pr^{3+}$–OH ratios (peak area of O lattice/O total or $Ti^{3+}/Pr^{3+}$–OH/O total peak area).

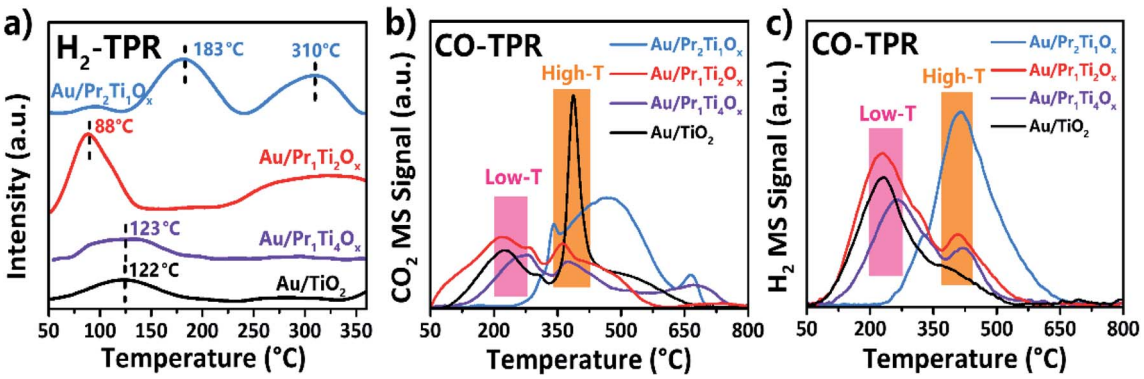


Fig. 9 (a) $H_2$-TPR (b and c) CO-TPR profiles of $Au/TiO_2$ and $Au/Pr_aTi_bO_x$ catalysts.

The DRIFT spectras of CO adsorption on $Au/TiO_2$, $Au/PrO_x$ and $Au/Pr_aTi_bO_x$ catalysts were used to further confirm the oxidation state of Au. As shown in Fig. 6(a), the absorption bands observed at $\nu = 2168$, 2166, 2170, 2174 and 2172 $cm^{-1}$ can be assigned to CO adsorbed on the oxide support ($TiO_2$, $PrO_x$ and $Pr_aTi_bO_x$). The bands at 2095, 2097, 2101 and 2099 $cm^{-1}$ can be assigned to CO adsorbed on $Au^0$ (Fig. 6(d)). The bands at 2122, 2120, 2123 and 2125 $cm^{-1}$ can be assigned to CO adsorbed on $Au^{\delta+}$ (Fig. 6(d)).[37] The CO adsorbed on $Pr_aTi_bO_x$ also shows the band at 2122 $cm^{-1}$, after loading Au on it ($Au/Pr_aTi_bO_x$), the peak intensity further increased indicates it is overlapped with the CO–$Au^{\delta+}$ band. Fig. 6(d) shows the enlarged CO–$Au^{\delta+}$ and CO–$Au^0$ band on all the samples. As we can see the intensity of CO–$Au^{\delta+}$ and CO–$Au^0$ band on $Au/TiO_2$ are the highest followed by $Au/Pr_1Ti_2O_x$ > $Au/Pr_2Ti_1O_x$ > $Au/Pr_1Ti_4O_x$ > $Au/PrO_x$. From the literature we know it has been intensively disputed whether metallic ($Au^0$) or ionic gold (cationic $Au^{\delta+}$ or anionic $Au^{\delta-}$) are the active site for WGSR.[22,25,51] For example, Stere *et al.* used the *in situ* DRIFTS coupled with plasma activation method and pointed that metallic Au was the most stable

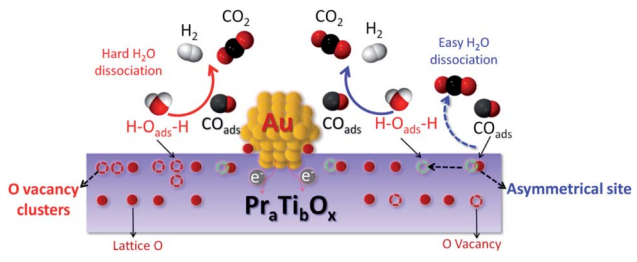


Fig. 10 Schematic illustration of the $H_2O$ dissociation on the asymmetrical O vacancy site and the following steps for WGSR.

Table 2 Comparison of catalytic performances toward WGSR over various gold-based catalysts

| Catalysts | Au (wt%) | Temp. (°C) | Gas feed composition | Reaction rate ($mol_{CO}$ $mol_{Au}^{-1}$ $s^{-1}$) | Ref. |
|---|---|---|---|---|---|
| $Au/TiO_2$ | 1 | 300 | 2% CO–10% $H_2O$–$N_2$ | 0.077 | This work |
| $Au/Pr_1Ti_4O_x$ | 1 | 300 | 2% CO–10% $H_2O$–$N_2$ | 0.092 | This work |
| $Au/Pr_1Ti_2O_x$ | 1 | 300 | 2% CO–10% $H_2O$–$N_2$ | 0.327 | This work |
| $Au/Pr_2Ti_1O_x$ | 1 | 300 | 2% CO–10% $H_2O$–$N_2$ | 0.022 | This work |
| $Au/Pr(OH)_x$–M | 1 | 350 | 2% CO–10% $H_2O$–$N_2$ | 0.502 | 12 |
| $Au/PrO_x$ | 1 | 350 | 2% CO–10% $H_2O$–$N_2$ | 0.024 | 12 |
| $Au/CeO_2$ | 4.7 | 250 | 11% CO–26% $H_2O$–26% $H_2$–7% $CO_2$–He | 0.127 | 24 |
| $Au@TiO_{2-x}$/ZnO | 2 | 250 | 6% CO–25% $H_2O$–Ar | 0.150 | 25 |
| $Au/TiO_2$ | 2 | 227 | 1% CO–3% $H_2O$–He | 0.030 | 45 |
| $Au/CeO_2$ | 3 | 163 | 4.5% CO–13.5% $H_2O$–He | 0.033 | 61 |
| $Au/TiO_2$ | 2.3 | 120 | 6.8% CO–11% $H_2O$–37.5% $H_2$–8.6% $CO_2$ | 0.011 | 62 |
| $Au/\alpha$-$Mo_2C$ | 2 | 150 | 11% CO–26% $H_2O$–26% $H_2$–7% $CO_2$–$N_2$ | 1.050 | 63 |
| $Au/Mo_2C$ | 1.5 | 120 | 7% CO–22% $H_2O$–8.5% $CO_2$–37% $H_2$–Ar | 0.020 | 64 |
| $Au/TiO_{2-x}$ | 1.95 | 200 | 6% CO–25% $H_2O$–Ar | 0.040 | 65 |
| $Au/ZrO_2$–$H_2$ | 3.8 | 210 | 6.25% CO–50% $H_2O$–$N_2$ | 0.405 | 66 |
| Au/CeFeAl | 2.17 | 250 | 4.5% CO–30% $H_2O$–$N_2$ | 0.026 | 67 |

and active species, the $Au^{\delta+}$ is less active for the WGSR in the Au/$CeZrO_4$ catalyst.[51] Jia *et al.* reported that CO–$Au^0$ was not the active site for the WGSR due to its inferior ability for CO adsorption under the WGSR conditions. The CO–$Au^{\delta+}$ species at interfaces make the real contributions for the gold–ceria catalyst.[22] While Wei *et al.* reported that the $Au^{\delta-}$ induced through a strong electronic metal–support interaction (EMSI) between Au and $TiO_{2-x}$ acts as an active site for CO chemisorptions on the $Au@TiO_{2-x}$/ZnO catalyst in WGSR.[25] Based on the current work, it's hard to say whether pure $Au^0$, $Au^{\delta+}$ and $Au^{\delta-}$ are the active sites. But it can be sure that the CO adsorbed on Au or the Au-support interface indeed play an important role in WGSR, as CO can also adsorb on the pure oxides but almost no WGS reactivity on the pure oxides. Although the intensity of CO on $Au/Pr_1Ti_2O_x$ is in medium among all the catalysts, it shows the highest reactivity. One explanation is that following the "Sabatier principle", the CO should have the "just right" interactions with Au or Au-support interface which should neither too strong nor too weak, can easily react with the OH group in the following steps.

To further clarify the electronic interactions between Ti and Pr, we explored the valence changes in both Ti and Pr caused by the mixing of them. Fig. 7(a) and (b) shows the Pr 3d and Ti 2p XPS spectra of the $Au/Pr_aTi_bO_x$ and $Au/TiO_2$ catalysts after WGSR. Due to the complex nature of final-state effects in the Pr 3d systems (hybridization of $4f^2$ and $4f^3\underline{L}$ ($\underline{L}$ hole) and the multiple coupling of unpaired 4f electrons with 3d hole), distinguishing between $Pr^{3+}$ and $Pr^{4+}$ by XPS is challenging.[9,13,14,52–54] The systematic studies of praseodymium oxides from Schaefer *et al.* point the peaks intensity increased at 973 and 949 eV after oxygen plasma treatment under UHV condition.[52] The ratio of these peaks therefore can be used as a semi-quantitative probe for the amount of $Pr^{3+}$ in the oxides (Fig. S3†). The two peaks centered at 954 and 934 eV due to hybridization of O 2p and Pr 4f can be attributed to $Pr^{4+}$. The Ti $2p_{3/2}$ spectrum in Fig. 7(b) is deconvoluted into three peaks at 459.8, 458.5 and 457.2 eV, assigned to the $Ti^{2+}$, $Ti^{3+}$ and $Ti^{4+}$ states, respectively.[9,25,55,56]

Fig. 7(c) depicts changes of $Ti^{2+}$, $Pr^{3+}$ and $Pr^{4+}$ content with the mixing of Pr : Ti from 1 : 4 to 1 : 2 and 2 : 1. As we can see, the ratios of $Ti^{2+}$ and $Pr^{4+}$ following the same trend, with the $Au/Pr_1Ti_2O_x$ has the highest amount of $Ti^{2+}$ (0.16) and $Pr^{3+}$ (0.30), also corresponding the lowest amount of $Pr^{4+}$ (0.70). This can be explained by the interaction between Pr and Ti. It is known that in $TiO_2$ the main cations are $Ti^{4+}$, while in $PrO_x$ the majority of cations are $Pr^{3+}$. As $Ti^{4+}$ (0.745 Å) is smaller than $Pr^{3+}$ (1.266 Å), it should have a stronger affinity to electrons, when both $Ti^{4+}$ and $Pr^{3+}$ coordinate with O (Ti–O–Pr).[6,13,25] Electrons of O may tend to move to Ti, leading to the reduction of $Ti^{4+} \rightarrow Ti^{2+}$ (accompanied by the creation of O vacancies). Simultaneously, the O attracts more electrons from Pr for compensation result in the oxidation of $Pr^{3+}$ to $Pr^{4+}$. However, the content of $Ti^{2+}$ and $Pr^{4+}$ doesn't monotonously increase with the amount of Ti in the mixed oxides. This can be explained by an asymmetry effect of the chemical bonds in Fig. 7(d). Recently, Zhou and co-workers proposed that the asymmetric $A_{metal}$–O–$(B_{metal})_x$ led to easier O vacancy formation, which is accompanied by electron transformation between metals.[17]

XPS spectroscopy was also used to study changes in surface oxygen vacancies, induced by mixing of Ti and Pr. According to Hyuntae *et al.*, the O 1s could be deconvoluted into 3 peaks.[57] The binding energy of around 529.5 eV is attributed to the lattice oxygen of $Ti^{4+}$–$O_2$ or $Pr^{4+}$–$O_2$.[12,25,56] The peak at 533.5 eV can be ascribed to adsorbed (molecular) $H_2O$ (surface hydroxyl-like groups).[57] Features near 531.7 eV originate from $Pr^{3+}$–OH or $Ti^{3+}$–OH, *i.e.*, the reactant water dissociated on O vacancies ($O^{\#}$). As these species indicate the abundance of $O^{\#}$, they have also been labeled $O_V$ in the literature.[57–59] In the current case, for the higher Pr amounts, the 531.7 eV peak mostly originates from $Pr^{3+}$–OH (Fig. 8(a)).[57]

The ratio of surface oxygen vacancies and lattice O is compared in Fig. 8(b). It can be seen that after adding

praseodymium into titanium oxide the O vacancies ratio increased greatly, meanwhile the ratio of lattice O decreased. With $Au/Pr_2Ti_1O_x$ has the highest O vacancy ratio (0.68) followed by $Au/Pr_1Ti_2O_x$ (0.50) > $Au/Pr_1Ti_4O_x$ (0.38) > $Au/TiO_2$ (0.22). The theory study points that O vacancies play a key role in $H_2O$ dissociation which is known as the limiting step for WGSR.[60] Our catalytic test shows that $Au/Pr_1Ti_2O_x$ has the highest catalytic activity, however, the $Au/Pr_1Ti_4O_x$ exhibits much lower activity and the $Au/Pr_2Ti_1O_x$ has almost no reactivity, although the latter two catalysts also contain a high amount of oxygen vacancies. This indicates other factors such as the chemical environment of oxygen vacancies play a more important role in determining its reactivity. According to Zhou *et al.* in the mixed oxides such as $Ce_{1-x}Bi_xO_{2-\delta}$ the asymmetrical oxygen vacancies will be formed, which prefer to be filled by adsorbed oxygen species, due to a local charge balance or stable coordination for $Ce^{4+}$.[16] More importantly, the filled oxygen in these sites is also more easily to be released due to the asymmetric bonding effect.

The activity of surface O and OH was further investigated by $H_2$-TPR and CO-TPR. The $H_2$ TPR in Fig. 9(a) shows the $H_2$ consumption peak on four catalysts. The reduction peak on $Au/Pr_1Ti_2O_x$ appears at 88 °C, which is much lower than other samples such as $Au/Pr_2Ti_1O_x$ at 183 and 310 °C, $Au/Pr_1Ti_4O_x$ and $Au/TiO_2$ at 123 °C. Moreover, the peak intensity is also much higher than other samples (2.4 times of $Au/Pr_1Ti_4O_x$ and $Au/TiO_2$). The relatively low $T$ of $H_2$ consumption on $Au/Pr_1Ti_2O_x$ indicates the easy release of surface O. This can be attributed to two reasons: one is due to the weakening of Pr–O or Ti–O bond in $Au/Pr_1Ti_2O_x$ caused by the asymmetrical chemical environment, the EXAFS and DFT studies by Dutta *et al.* show that substitution of Ce by another metal ion (Ti) can create disorder in the crystalline structure, resulting in the formation of weak long M–O bonds, similarly the distortion in $Pr_1Ti_2O_x$ can also lead to the formation of long M–O bonds; the other one is the weakened O species bond contiguous to Au at the interface can further facilitates the O reduction.

After CO exposure, the CO-TPR (mass 44) in Fig. 9(b) shows that the $CO_2$ desorption peaks can be divided into two groups, the low-temperature group (50–350 °C) and the high-temperature group (350–800 °C), they are accompanied by the evolution of hydrogen in Fig. 9(b) (mass 2). The $H_2$ production can be ascribed to the WGSR from the adsorbed CO reacts with hydroxyl groups on the surface. As can be seen in Fig. 9(b) and (c), in the low-temperature range the amount of $CO_2$ and $H_2$ is also in line with catalytic test with $Au/Pr_1Ti_2O_x$ is the highest followed with $Au/TiO_2$ > $Au/Pr_1Ti_4O_x$ > $Au/Pr_2Ti_1O_x$. No obvious $H_2$ peak appears at the high-temperature range. Therefore, it could be due to the Au-catalyzed abstraction of the bulk lattice oxygen over oxides support by CO.

As illustrated in Fig. 10 after removing the active O species by CO (in WGSR) the asymmetrical O vacancy will be exposed. The asymmetrical O vacancy is energetically quite unstable tend to adsorb and dissociate $H_2O$ more easily compared with other types of O vacancies (like O vacancy clusters). To be noted the experimentally directly distinguish the asymmetrical O vacancy site are difficult, more works are still needed to be done.

In WGSR, CO will first react with the active surface O species, thereby exposing the asymmetrical oxygen vacancies, and which will absorb water molecular and dissociate it into H and OH groups. The generated OH groups can react with CO, yielding $CO_2$ and $H_2$ (final products of WGSR). The entire pathway is summarized below:

$$CO(a) + O\ (\text{asymmetrical site}) \rightarrow CO_2 + O\ \text{vacancy}\ (\text{asymmetrical})$$

$$H_2O(a) + O\ \text{vacancy}\ (\text{asymmetrical}) \rightarrow OH(a) + H(a)$$

$$CO(a) + OH(a) \rightarrow HOCO(a)$$

$$HOCO(a) \rightarrow CO_2 + H(a)$$

$$2H(a) \rightarrow H_2$$

# 4. Conclusions

In this work, praseodymia–titania solid solutions with different mixing ratios have been prepared *via* a sol–gel method. $Au/Pr_1Ti_2O_x$ exhibits the better reaction rate (0.327 $mol_{CO}$ $mol_{Au}^{-1}$ $s^{-1}$) in comparison to gold-based catalysts reported previously (Table 2).[15,45,61–67] The TOFs of $Au/Pr_1Ti_2O_x$ is as high as 4.02 $s^{-1}$ at 300 °C and it also exhibits good long-term stability within the 40 h continues test only lost 8% activity (300 °C) in WGSR. The HRTEM and STEM revealed that the Au nanoparticles with the mean size of 3.0 ± 1.2 nm in $Au/Pr_1Ti_2O_x$ are half embedded in the $Pr_2Ti_1O_x$ support. By varying the Pr ratio in the mixed oxides, the valence state of the supported Au species ($Au^+$ and Au) and the amount of $Ti^{2+}$, $Pr^{3+}$, $Pr^{4+}$ changed, which corresponds to an electronic interaction of Au and $Pr_aTi_bO_x$ and a valence compensation effect between Ti and Pr, respectively. CO-DRIFT confirmed the adsorption CO on Au and Au–support interfacial sites. The XPS study demonstrates by increasing the amount of Pr doping the number of oxygen vacancies increase, however, don't lead to the corresponding increase of the catalytic activity of $Au/Ce_aPr_bO_x$. This proved that the nature of or chemical environment the vacancy sites plays a more important role in affecting the catalytic activity rather than just their abundance. The $H_2$-TPR confirms the easier removal of O species from $Au/Pr_1Ti_2O_x$ due to the weakened Pr–O or Ti–O bond by the forming of an asymmetrical chemical environment. The exposed asymmetrical O vacancies due to reduction are more active, play a key role in the $H_2O$ dissociation in WGSR. This research provides a new way to design and modulate the active sites in catalysts from the point of adjusting the chemical environment and gives a comprehensive understanding of the structure–function relation of mixed oxides supported Au catalysts.

# Author contributions

Weixuan Zhao performed the preparation of catalysts, doing the catalysis test. The BET, ICP, TEM and XPS characterizations were performed in Shiyanjia Lab (https://www.shiyanjia.com).

Junjie Shi and Weixuan Zhao wrote the manuscript, prepared the figures and analyzed the data. Junjie Shi designed and supervised the project. MingYue Lin and Toru Murayama helped with CO-DRIFTS characterization and analysis. Libo Sun, Xun Sun and Huijuan Su helped modify the manuscript. Caixia Qi involved in the modification of the manuscript and provided great support for the project.

## Conflicts of interest

The authors declare no conflict of interest.

## Acknowledgements

Junjie Shi gratefully acknowledges the financial support of the National Science Foundation of China for Young Scholar (21902141) and the Natural Science Foundation of Shandong Province (ZR2018QB006). We also acknowledge the financial supports from the Collaborative Innovation Center of Light Hydrocarbon Transformation and Utilization of Yantai University.

## References

1 A. Puigdollers, P. Schlexer, S. Tosoni and G. Pacchioni, *ACS Catal.*, 2017, **7**, 6493–6513.
2 E. McFarland and H. Metiu, *Chem. Rev.*, 2013, **113**, 4391–4427.
3 I. Wachs and K. Routray, *ACS Catal.*, 2012, **2**, 1235–1246.
4 J. Sattler, J. Ruiz-Martinez, E. Santillan-Jimenez and B. Weckhuysen, *Chem. Rev.*, 2014, **114**, 10613–10653.
5 I. Ro, J. Resasco and P. Christopher, *ACS Catal.*, 2018, **8**, 7368–7387.
6 D. Stacchiola, S. D. Senanayake, P. Liu and J. A. Rodriguez, *Chem. Rev.*, 2013, **113**, 4373–4390.
7 F. Polo-Garzon, Z. Bao, X. Zhang, W. Huang and Z. Wu, *ACS Catal.*, 2019, **9**, 5692–5707.
8 M. Ganduglia-Pirovano, A. Hofmann and J. Sauer, *Surf. Sci. Rep.*, 2007, **62**, 219–270.
9 Q. Xiao, Y. Wang, Z. Zhao, C. Pei, S. Chen, L. Gao, R. Mu, Q. Fu and J. Gong, *Sci. China: Chem.*, 2020, **63**, 1323–1330.
10 P. Sonström, J. Birkenstock, Y. Borchert, L. Schilinsky, P. Behrend, K. Gries, K. Müller, A. Rosenauer and M. Bäumer, *ChemCatChem*, 2010, **2**, 694–704.
11 J. Shi, A. Wittstock, C. Mahr, M. Murshed, T. Gesing, A. Rosenauer and M. Bäumer, *Phys. Chem. Chem. Phys.*, 2019, **21**, 3278–3286.
12 J. Shi, H. Li, W. Zhao, P. Qi and H. Wang, *Catal. Sci. Technol.*, 2020, **10**, 7291–7301.
13 G. Niu, M. Zoellner, T. Schroeder, A. Schaefer, J. Jhang, V. Zielasek, M. Bäumer, H. Wilkens, J. Wollschlager, R. Olbrich, C. Lammers and M. Reichling, *Phys. Chem. Chem. Phys.*, 2015, **17**, 24513–24540.
14 H. Wilkens, S. Gevers, S. Röhe, A. Schaefer, M. Bäumer, M. Zoellner, T. Schroeder and J. Wollschläger, *J. Phys. Chem. C*, 2014, **118**, 3056–3061.
15 J. Shi, H. Li, A. Genest, W. Zhao, P. Qi, T. Wang and G. Rupprechter, *Appl. Catal., B*, 2022, **301**, 120789.
16 K. Yu, D. Lei, Y. Feng, H. Yu, Y. Chang, Y. Wang, Y. Liu, G. Wang, L. Lou, S. Liu and W. Zhou, *J. Catal.*, 2018, **365**, 292–302.
17 K. Yu, L. Lou, S. Liu and W. Zhou, *Adv. Sci.*, 2020, **7**, 1901970.
18 Z. Han, Y. Yang, B. Zhu, M. Ganduglia-Pirovano and Y. Gao, *Phys. Rev. Mater.*, 2018, **2**, 035802.
19 M. Wolf, C. Castleton, K. Hermansson and J. Kullgren, *Front. Chem.*, 2019, **7**, 212.
20 J. Kullgren, M. Wolf, C. Castleton, P. Mitev, W. Briels and K. Hermansson, *Phys. Rev. Lett.*, 2014, **112**, 156102.
21 S. Rodriguez, P. Liu, J. Hrbek, J. Evans and M. Pérez, *Science*, 2007, **318**, 1757–1759.
22 X. Fu, L. Guo, W. Wang, C. Ma, C. Jia, K. Wu, R. Si, L. Sun and C. Yan, *J. Am. Chem. Soc.*, 2019, **141**, 4613–4623.
23 J. Rodriguez, P. Liu, J. Hrbek, J. Evans and M. Perez, *Angew. Chem., Int. Ed.*, 2007, **46**, 1329–1332.
24 Q. Fu, H. Saltsburg and M. Flytzani-Stephanopoulos, *Science*, 2003, **301**, 935–938.
25 N. Liu, M. Xu, Y. Yang, S. Zhang, J. Zhang, W. Wang, L. Zheng, S. Hong and M. Wei, *ACS Catal.*, 2019, **9**, 2707–2717.
26 L. Sun, J. Xu, X. Liu, B. Qiao, L. Li, Y. Ren, Q. Wan, J. Lin, S. Lin, X. Wang, H. Guo and T. Zhang, *ACS Catal.*, 2021, **11**, 5942–5950.
27 J. Dong, Q. Fu, Z. Jiang, B. Mei and X. Bao, *J. Am. Chem. Soc.*, 2018, **140**, 13808–13816.
28 J. Yang, X. Wang, Y. Qu, X. Wang, H. Huo, Q. Fan, J. Wang, L. Yang and Y. Wu, *Adv. Energy Mater.*, 2020, **10**, 2001709.
29 X. Wang and L. Yang, *Appl. Surf. Sci.*, 2022, **576**, 151839.
30 M. Zhu, C. Zhao, X. Liu, X. Wang, F. Zhou, J. Wang, Y. Hu, Y. Zhao, T. Yao, L. Yang and Y. Wu, *ACS Catal.*, 2021, **11**, 3923–3929.
31 X. Wang and L. Yang, *J. Mater. Chem. A*, 2022, **10**, 1481–1496.
32 J. Yang, Z. Wang, C. Huang, Y. Zhang, Q. Zhang, C. Chen, J. Du, X. Zhou, Y. Zhang, H. Zhou, L. Wang, X. Zheng, L. Gu, L. Yang and Y. Wu, *Angew. Chem., Int. Ed.*, 2021, **60**, 22722–22728.
33 C. Huang, G. Li, L. Yang and E. Ganz, *ACS Appl. Mater. Interfaces*, 2021, **13**, 608–621.
34 M. Zhao, B. Song and L. Yang, *ACS Appl. Mater. Interfaces*, 2021, **13**, 26109–26122.
35 J. Shi, C. Mahr, M. Murshed, V. Zielasek, A. Rosenauer, T. Gesing, M. Bäumer and A. Wittstock, *Catal. Sci. Technol.*, 2016, **6**, 5311–5319.
36 M. Lin, B. An, N. Niimi, Y. Jikihara, T. Nakayama, T. Honma, T. Takei, T. Shishido, T. Ishida, M. Haruta and T. Murayama, *ACS Catal.*, 2019, **9**, 1753–1756.
37 M. Lin, C. Mochizuki, B. An, Y. Inomata, T. Ishida, M. Haruta and T. Murayama, *ACS Catal.*, 2020, **10**, 9328–9335.
38 M. Lin, C. Mochizuki, B. An, T. Honma, M. Haruta, T. Ishida and T. Murayama, *J. Catal.*, 2020, **389**, 9–18.
39 W. Li, F. Wang, S. Feng, J. Wang, Z. Sun, B. Li, Y. Li, J. Yang, A. Elzatahry, Y. Xia and D. Zhao, *J. Am. Chem. Soc.*, 2013, **135**, 18300–18303.

40 T. Andana, M. Piumetti, S. Bensaid, L. Veyre, C. Thieuleux, N. Russo, D. Fino, E. Quadrelli and R. Pirone, *Appl. Catal., B*, 2018, **226**, 147–161.
41 L. Jiang, S. Fernandez-Garcia, M. Tinoco, Z. Yan, Q. Xue, G. Blanco, J. Calvino, A. Hungria and X. Chen, *ACS Appl. Mater. Interfaces*, 2017, **9**, 18595–18608.
42 J. Shi, A. Schaefer, A. Wichmann, M. Murshed, T. Gesing, A. Wittstock and M. Bäumer, *J. Phys. Chem. C*, 2014, **118**, 29270–29277.
43 J. Shi, C. Mahr, M. Murshed, T. M. Gesing, A. Rosenauer, M. Bäumer and A. Wittstock, *Phys. Chem. Chem. Phys.*, 2017, **19**, 8880–8888.
44 N. Ta, J. Liu, S. Chenna, P. Crozier, Y. Li, A. Chen and W. Shen, *J. Am. Chem. Soc.*, 2012, **134**, 20585–20588.
45 R. Si, J. Tao, J. Evans, J. Park, L. Barrio, J. Hanson, Y. Zhu, J. Hrbek and J. Rodriguez, *J. Phys. Chem. C*, 2012, **116**, 23547–23555.
46 W. Deng and M. Flytzani-Stephanopoulos, *Angew. Chem., Int. Ed.*, 2006, **45**, 2285–2289.
47 Y. Zhang, J. Zhang, B. Zhang, R. Si, B. Han, F. Hong, Y. Niu, L. Sun, L. Li, B. Qiao, K. Sun, J. Huang and M. Haruta, *Nat. Commun.*, 2020, **11**, 558.
48 T. Murayama and M. Haruta, *Chin. J. Catal.*, 2016, **37**, 1694–1701.
49 S. Wei, X. Fu, W. Wang, Z. Jin, Q. Song and C. Jia, *J. Phys. Chem. C*, 2018, **122**, 4928–4936.
50 C. Buergel, N. Reilly, G. Johnson, R. Mitric, M. Kimble, A. Castleman and V. Bonacic-Kouteckv, *J. Am. Chem. Soc.*, 2008, **130**, 1694–1698.
51 C. Stere, J. Anderson, S. Chansai, J. Delgado, A. Goguet, W. Graham, C. Hardacre, S. Taylor, X. Tu, Z. Wang and H. Yang, *Angew. Chem., Int. Ed.*, 2017, **56**, 5579–5583.
52 A. Schaefer, S. Gevers, V. Zielasek, T. Schroeder, J. Falta, J. Wollschlager and M. Bäumer, *J. Chem. Phys.*, 2011, **134**, 054701.
53 S. Lutkehoff, M. Neumann and A. Slebarski, *Phys. Rev. B: Condens. Matter Mater. Phys.*, 1995, **52**, 13808–13811.
54 H. Ogasawara, A. Kotani, R. Potze, G. Sawatzky and B. Thole, *Phys. Rev. B: Condens. Matter Mater. Phys.*, 1991, **44**, 5465–5469.
55 D. Wang, J. Huang, F. Liu, X. Xu, X. Fang, J. Liu, Y. Xie and X. Wang, *Catal. Today*, 2020, **339**, 220–232.
56 B. Bharti, S. Kumar, H. N. Lee and R. Kumar, *Sci. Rep.*, 2016, **6**, 32355.
57 H. Sohn, G. Celik, S. Gunduz, D. Dogu, S. Zhang, J. Shan, F. Tao and U. Ozkan, *Catal. Lett.*, 2017, **147**, 2863–2876.
58 C. Wen, Y. Zhu, Y. Ye, S. Zhang, F. Cheng, Y. Liu, P. Wang and F. Tao, *ACS Nano*, 2012, **6**, 9305–9313.
59 Z. Liu, T. Duchon, H. Wang, D. Grinter, I. Waluyo, J. Zhou, Q. Liu, B. Jeong, E. Crumlin, V. Matolin, D. Stacchiola, J. Rodriguez and S. Senanayake, *Phys. Chem. Chem. Phys.*, 2016, **18**, 16621–16628.
60 K. Sun, M. Kohyama, S. Tanaka and S. Takeda, *J. Phys. Chem. C*, 2017, **121**, 12178–12187.
61 F. Vindigni, M. Manzoli, T. Tabakova, V. Idakiev, F. Boccuzzi and A. Chiorino, *Phys. Chem. Chem. Phys.*, 2013, **15**, 13400–13408.
62 J. Wang, V. Kispersky, W. Delgass and F. Ribeiro, *J. Catal.*, 2012, **289**, 171–178.
63 S. Yao, Z. Xiao, Z. Wu, G. Rui, W. Xu, Y. Ye, L. Lin, X. Wen, P. Liu and B. Chen, *Science*, 2017, **357**, 389.
64 K. Sabnis, Y. Cui, M. Akatay, M. Shekhar, W. Lee, J. Miller, W. Delgass and F. Ribeiro, *J. Catal.*, 2015, **331**, 162–171.
65 P. Yin, J. Yu, L. Wang, J. Zhang, Y. Jie, L. Chen, X. Zhao, H. Feng, Y. Yang, M. Xu, X. Zhang, J. Han, H. Yan and M. Wei, *J. Phys. Chem. C*, 2021, **125**, 20360–20372.
66 L. Song, X. Cao and L. Li, *ACS Appl. Mater. Interfaces*, 2018, **10**, 31249–31259.
67 M. Castaño, T. Reina, S. Ivanova, M. Centeno and J. Odriozola, *J. Catal.*, 2014, **314**, 1–9.